Mechanisms and Kinetic Modeling of Calcium Oxalate Crystal Aggregation in a Urinelike Liquor

Part II: Kinetic Modeling

A general form of the population balance equation, including aggregation and rupture terms, was solved numerically to model the experimental calcium oxalate distributions generated in Part I of this series. Semiempirical formulations for the aggregation and disruption functions were found that resulted in excellent matches between experimental and predicted distributions. Both the aggregation and the disruption rates were found to vary with oxalate concentration and inner cylinder rpm of the aggregator.

R. W. Hartel and A. D. Randolph
Department of Chemical Engineering
University of Arizona
Tucson, AZ 85721

SCOPE

One of the most important factors in the formation of kidney stones from calcium oxalate crystals involves the aggregation of the individual crystals, as evidenced by the polycrystalline structure of large surgically removed stones. The aggregation rates of the calcium oxalate crystals depend on many factors, including the calcium and oxalate concentrations and the flow conditions in the kidney. A fundamental study of the influence of oxalate concentration and flow intensity on the aggregation of calcium oxalate crystals would have important implications concerning the major cause of stone formation and would help in the formulation of realistic models of kidney stone formation.

The aggregation of calcium oxalate crystals was studied experimentally using a continuous Couette-flow aggregator, as presented in Part I of this series. The objective of Part II was to model the experimental distributions using a general form of the population balance equation, including kinetic expressions for aggregation and disruption. Computer solution of this equation follows the technique employed by Gelbard (1981) for study of aerosol aggregation and provides qualitative information concerning the relative rates of aggregation and disruption.

The effects on aggregation of the flow field intensity and the oxalate concentration were studied. These parameters represent two major factors believed to be important in the formation of kidney stones.

CONCLUSIONS AND SIGNIFICANCE

The population balance equation was solved numerically and compared to the experimental distributions of calcium oxalate crystals generated in Part I of this series using semiempirical formulations for aggregation and disruption. The model distributions matched well with the experimental distributions for various oxalate concentrations and inner cylinder rotation rates.

Several theoretical aggregation kernels were employed, including formulations for laminar flow and turbulent flow fields, that did not model the general shape of the experimental distribution. An empirical aggregation kernel was found that matched the experimental distributions throughout the range of flow conditions and oxalate concentrations used. A simple two-body

equal-volume disruption function was found to model the experimental distributions for the majority of the data. A more sophisticated formulation would be necessary only at the highest levels of agitation.

The aggregation rate was found to be a strong function of the oxalate concentration in the aggregator. Presumably, the change in the ionic conditions at the crystal surface enhanced the probability of two particles staying together upon collision. This also resulted in the decrease in the disruption rate as the oxalate concentration increased. This suggests that at the higher oxalate concentrations, the coagulation mechanism becomes more agglomerationlike due to the stronger bonding between crystals. The clinical implications for kidney stone prevention are that the oxalate concentration is an important variable for control of stone formation; at low levels of oxalate it is less likely that stable agglomerates will form from loosely bound aggregates.

The flow field intensity (inner cylinder rpm of the agglomerator) was found to have very little effect on the aggregation rate at 0.6 mM oxalate concentration. At increased oxalate concentrations, however, the effect of increased rotation rate was to lower the aggregation rate. At the same time, the disruption rate increased significantly with the rotation rate. Even though agitation levels in this study were significantly higher than physiological conditions, the shear rate and oxalate concentration kinetics presented in this paper should be of interest in formulating models of stone disease. The experimental apparatus and population balance data analysis should prove useful in the kinetic modeling of agglomeration and aggregation in other chemical systems.

Introduction

Kidney stones are often observed to be polycrystalline aggregates of various mineral salts. It is reasonable, then, to suspect that agglomeration/aggregation phenomena play a significant role in the overall mechanism of kidney stone formation. (Current ASTM terminology for agglomeration and aggregation is employed in this paper. For further clarification, see the introduction to Part I.) In order to study this phenomenon, a continuous, two-stage crystallization apparatus was employed. Calcium oxalate (CaOx) nuclei from a mixed-suspension, mixed-product-removal (MSMPR) nucleator were aggregated in a Couette-flow apparatus. By this procedure, aggregation could be studied independently of crystal growth and nucleation. In Part I it was shown that these small (predominantly $<30\ \mu m$) CaOx crystals grown from urinelike solutions would readily aggregate in the shear flow field of the Couette-flow aggregator. Changes in the crystal size distribution (CSD) in the aggregator were attributed to both aggregation of the CaOx nuclei and to the subsequent rupture of the newly formed aggregates in the flow field. Aggregate disruption was found to correlate well with the onset of turbulence in the flow field of the aggregator. These experimental results showed that the aggregation rate increased with the inner cylinder rpm and the oxalate concentration of the Couette-flow aggregator. The rupture of the newly formed aggregates was observed to increase as the flow field intensity (inner cylinder rpm) increased, and to decrease as the oxalate concentration increased. For further details of the experimental apparatus and results, see Part I and Gottung (1983).

The purpose of the present paper was to empirically model the experimentally determined aggregator distributions presented in Part I. The population balance equation with quantitative kinetic expressions for aggregation and disruption was solved numerically to model the experimental distributions. Evaluation of the relative rates of aggregation and rupture provides a means of distinguishing between aggregation (the formation of loosely bound particle clusters) and agglomeration (the formation of more tightly cemented particle clusters). The dependence of these rates on the shear field and the oxalate concentration in the aggregator can aid in elucidating the actual mechanism for formation of kidney stones.

Theory

The general form of the population balance equation in volume coordinates is

$$\frac{\partial n}{\partial t} + \frac{\partial}{\partial v}(nG_v) + \frac{n - n_i}{\tau} = B_a - D_a + B_d - D_d + \int_o^\infty \delta(v - v_a)\, B_u\, dv \quad (1)$$

where $B_a - D_a$ and $B_d - D_d$ represent the net formation of particles at a size v by aggregation and rupture, respectively. The addition of mass B_u at the lowest measurable size, v_a, is necessary to account for the growth and aggregation of these particles into the measurable size range. The aggregation of two particles of size μ and $v - u$ into a particle of size v can be written as (Drake, 1972; Swift and Friedlander, 1964)

$$B_a = \frac{1}{2}\int_o^v K(u, v - u)n(u, t)n(v - u, t)du \quad (2)$$

and

$$D_a = n(v, t)\int_o^\infty K(u, v)n(u, t)du \quad (3)$$

The formulation of the aggregation kernel, $K(u, v)$, is chosen to correspond to the particular mechanism of aggregation. It accounts for the physical forces that describe the aggregation process.

The feed distribution, n_i, to the aggregator was the product distribution of the mininuclear. It was found to be an exponential distribution in size as predicted by the simplified population balance equation for an MSMPR crystallizer. It was converted into volume coordinates using the chain rule. The volume growth rate, G_v, was taken to be the growth rate of crystals in the

mininucleator even though the ion concentrations in the aggregator were generally different. This value was used throughout due to the lack of accurate solution oxalate measurements in the urinelike liquor in the aggregator. The error caused by this uncertainty was generally less than 10%, due to the relatively large influences of aggregation and disruption.

Equations 1 through 3 were solved numerically to fit the experimental aggregator data in Part I. The formulations describing the aggregation kernel and the distribution functions, as well as the mass addition rate, B_u, were adjusted until the model distribution matched the experimental aggregator distributions.

Aggregation kernel

There are many formulations, both theoretical and empirical, for the aggregation kernel (Drake, 1972) that describe the various mechanisms of aggregation. Some of the more important formulations are tabulated in Table 1 and described in more detail as follows.

Smoluchowski (1917) showed that when spherical particles coagulate under the influence of Brownian motion, the collision frequency factor takes the form:

$$K(u, v) = \frac{2\kappa T}{3\mu} [u^{1/3} + v^{1/3}] [u^{-1/3} + v^{-1/3}] \qquad (4)$$

For monodisperse particles, $[u^{1/3} + v^{1/3}] [u^{-1/3} + v^{-1/3}] = 4$ and the aggregation kernel becomes independent of volume.

Smoluchowski also showed that for spherical particles coagulating in a laminar shear field, the aggregation kernel is expressed as

$$K(u, v) = \tfrac{4}{3}(Sh) [u^{1/3} + v^{1/3}]^3 \qquad (5)$$

In turbulent flow, two different collision mechanisms may operate (Levich, 1962). The collisions of particles entrained within the turbulent eddies due to a diffusion mechanism can be expressed as (Low, 1975)

$$K(u, v) = k_1 \dot{U} [u^{1/3} + v^{1/3}]^3 \qquad (6)$$

This turbulent diffusion formulation is similar to that given for aggregation in a laminar flow field. When the density of the coagulating particles is much greater than the density of the fluid, the particles may escape from the turbulent eddies and collide with other particles. Collisions due to this turbulent inertial mechanism have been given by Drake (1972) as:

$$K(u, v) = 0.2 \frac{\rho \epsilon^{3/4}}{\rho_o \nu^{5/4}} E_i (u^{1/3} + v^{1/3})^2 |u^{2/3} - v^{2/3}| \qquad (7)$$

Levich concludes that the inertial mechanism is the major influence in the aggregation rate of polydispersed aerosols with sizes larger than 0.1 to 1 μm, due to the large density differences between the particles and air. However, for the aggregation of colloids in turbulent fluid flow, collisions due to the diffusion of particles within the eddies is the dominant mechanism. In both cases it is assumed that the particles are smaller than the size scale of the turbulent eddies.

Several expressions have been developed for coagulation due to particle velocities caused by a gravitational field. The terminal velocity varies with particle size, causing collisions of different size particles. For small (<50 μm) particles, the terminal velocity is given by Stoke's law and the aggregation kernel is given as (Drake, 1972)

$$K(u, v) = C_A E_i (u^{1/3} + v^{1/3})^2 |u^{2/3} - v^{2/3}| \qquad (8)$$

Berry (1967) developed an aggregation kernel to describe the collisions of particles greater than 50 μm caused by gravitational influences. Berry's expression is given as:

$$K(u, v) = C_A E_i (u^{1/3} + v^{1/3})^2 |u^{1/3} - v^{1/3}| \qquad (9)$$

Thompson (1968) noted that Eq. 9 was not conducive to numerical analyses as it had a discontinuous derivative at $u = v$, and consequently replaced Berry's formulation with a single analytic approximation given as:

$$K(u, v) = C_A E_i (u - v)^2/(u + v) \qquad (10)$$

The solution of Eq. 1 becomes simpler when the semiempirical formulation of Eq. 10 is used rather than Eq. 9.

Table 1. Aggregation Kernels

Brownian motion (Smoluchowski, 1917)	$K(u, v) = \frac{2\kappa T}{3\mu} [u^{1/3} + v^{1/3}][u^{-1/3} + v^{-1/3}]$
Laminar shear (Smoluchowski, 1917)	$K(u, v) = \frac{4}{3} Sh [u^{1/3} + v^{1/3}]^3$
Turbulent diffusion (Low, 1975)	$K(u, v) = k_1 \dot{U} [u^{1/3} + v^{1/3}]^3$
Turbulent inertia (Drake, 1972)	$K(u, v) = 0.2 \frac{\rho \epsilon^{3/4}}{\rho \nu^{5/4}} \cdot E_i (u^{1/3} + v^{1/3})^2 (u^{2/3} - v^{2/3})$
Gravitational settling ($L < 50\mu$m) (Drake, 1972)	$K(u, v) = C_A E_i (u^{1/3} + v^{1/3})^2 \lvert u^{2/3} - v^{2/3} \rvert$
Gravitational settling ($L > 50$ μm) (Berry, 1967)	$K(u, v) = C_A E_i (u^{1/3} + v^{1/3})^2 \lvert u^{1/3} - v^{1/3} \rvert$
Semiempirical formulation (Thompson, 1968)	$K(u, v) = C_A E_i (v)^2/(u + v)$

Disruption function

Although many forms exist for the disruption terms B_d and D_d (Randolph and Larson, 1971; Petanate and Glatz, 1983), a particularly simple form which requires no integration of a fragment distribution function is the two-body equal-volume breakage function. It is assumed that one large particle breaks into two smaller pieces, each of half the original volume. For this simplified case, it follows that (Randolph and Larson):

$$B_d(v) = 2D_d(2v) \qquad (11)$$

Randolph (1969) proposed a form for D_d that was proportional

to the volume of the rupturing particle and the population density at that volume. Petanate and Glatz arrived at the same form through theoretical considerations assuming that local shear forces were responsible for the disruption. The disruption functions then become:

$$D_d = K_d\, n(v) \tag{12}$$

and

$$B_d = 4K_D\, v\, n(2v) \tag{13}$$

These forms were used in this study where the disruption parameter, K_D, was considered to be a function of both the flow field intensity (inner cylinder rpm) and the oxalate concentration in the aggregator. More complicated forms of B_d could have been used, forms that took into account the distribution of ruptured fragments. The simple form of Eq. 11 was adequate to model these data and required only iteration instead of integration when implemented in the population balance.

Source function

In Part I it was shown that the total volume (or total mass) of the aggregator distribution differed from that of the crystallizer distribution, depending on the experimental conditions. It was explained that this was an artifact of the measurement size range of the particle counter. Any crystals smaller than 5 μm were not measured. Since these particles less than 5 μm grew and aggregated in the aggregator, they became countable in the aggregator distribution and, in part, caused the change in total volume between aggregator and crystallizer distributions. In order to take this into account in the kinetic modeling, a source function, B_u, was incorporated into the population balance equation. This source term adds the volume of crystals to the smallest size increment used in the numerical analysis to account for any mass entering the aggregator distribution from below the smallest measurable size. It may also be dependent on rpm and/or oxalate concentration.

Numerical Analysis

The final form of the population balance equation is:

$$\frac{\partial n}{\partial t} + \frac{\partial}{\partial v}(n\,G_v) + \frac{n - n_i}{\tau} = \frac{1}{2}\int_o^v K(u, v-u)n(u)n(v-u)du - n(v)\int_o^v K(u,v)n(u)du + 4K_D v\, n(2v) - K_D v\, n(v) + \int_o^\infty \delta(v - v_o)B_u dv \tag{14}$$

Numerical solution of a general form of Eq. 14 has been reviewed by Gelbard and Seinfeld (1978). The computer code (program AEROSL) written by Gelbard (1980) incorporated a Gaussian-Legendre quadrature technique to evaluate the aggregation integrals, and an ordinary differential equation package to solve the resulting ordinary differential equation in time for each volume increment. The predictor-corrector technique for the solution of ordinary differential equations is discussed in detail by Shampine and Gordon (1975). Variables such as the aggregation kernel and the source and removal terms were input as separate user-written subroutines in program AEROSL.

In order to use program AEROSL, an initial distribution given by the crystallizer distribution was input into the program. AEROSL was then allowed to run until a steady state distribution was predicted. This point was reached when no further changes occurred in the predicted distribution. In general, the steady state distribution was attained after 4,000 s of aggregation time.

In order to fit the experimental distributions, a trial-and-error method was used to minimize the logarithmic sum-of-squares difference between the experimental and predicted aggregator distributions. A logarithmic sum-of-squares difference was employed since there was several orders of magnitude difference in population density between the smallest and largest crystals. This allowed the whole distribution to be accounted for with equal accuracy. Each of the parameters was varied until the lowest sum-of-squares difference was obtained.

Computational Results

Various formulations for the aggregation kernel were used in this study in an attempt to predict the aggregator distributions. These included simplified versions of the laminar shear field formulation and the turbulent mechanisms, as well as several empirical forms. Since the flow field in the aggregator changed from transitional to turbulent flow in the range of inner rpm's employed, it was expected that the laminar and/or turbulent formulations would be most successful. It was found that the formulation that most successfully fit the majority of the data was the analytic expression developed by Thompson (1968) given in Eq 10. The collection efficiency, E_i, was set equal to one and the aggregation constant C_A was found to be a function of both rpm and oxalate concentration.

Examples of the match between experimental and predicted distributions are shown in Figures 1–3. The fits at various higher

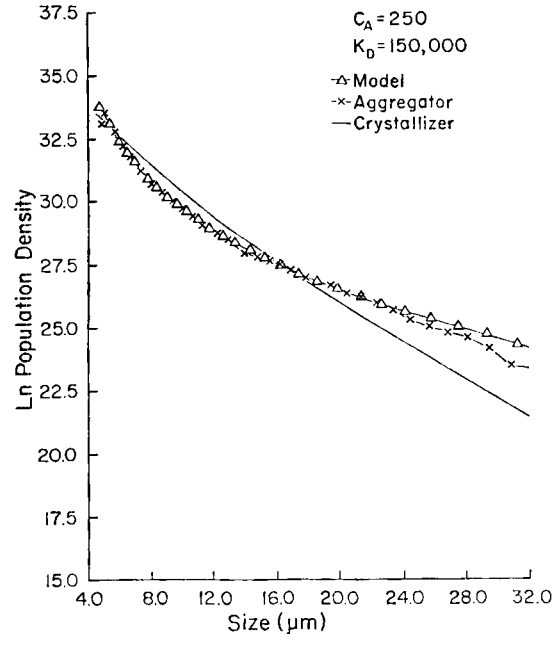

Figure 1. Comparison of calculated model distribution with experimental aggregator distribution at 80 rpm, 0.6 mM.

Experiment 3/14B, population density expressed in volume coordinates.

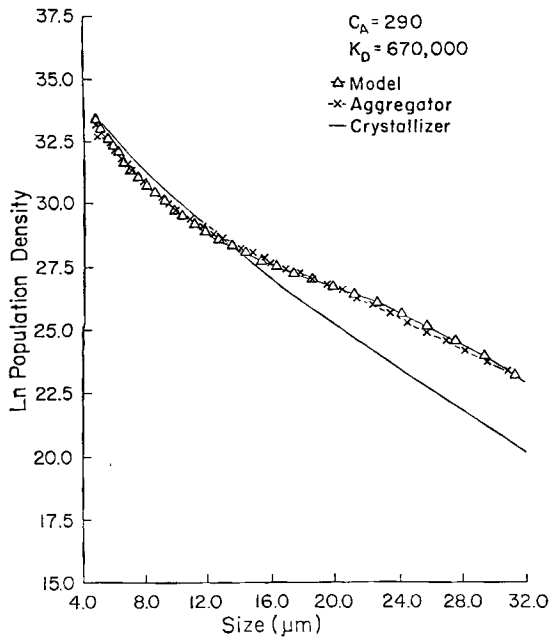

Figure 2. Comparison of calculated model distribution with experimental aggregator distribution at 150 rpm, 0.6 mM.

Experiment 3/23B, population density expressed in volume coordinates.

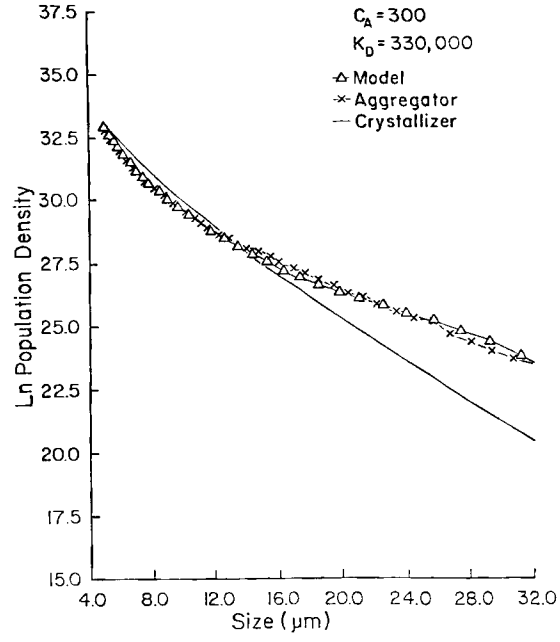

Figure 4. Comparison of calculated model distribution with experimental aggregator distribution at 150 rpm, 1.2 mM.

Experiment 5/8, population density in volume coordinates.

oxalate concentrations are shown in Figure 4–6. Tables 2 and 3 list the values of C_A, K_D, and B_u that gave the best fit for the distribution at the various conditions. The resulting logarithmic sum-of-squares differences from 5 to 30 μm are also given.

Several trends can be observed when these parameters are plotted as functions of inner cylinder rpm and oxalate concentration in the aggregator. Figure 7 shows how the aggregation constant varies with rpm. Within the error brackets representing the standard deviation of the parameters, there is no change in aggregation constant with rpm at this oxalate concentration. The change in the aggregator distribution appears to be

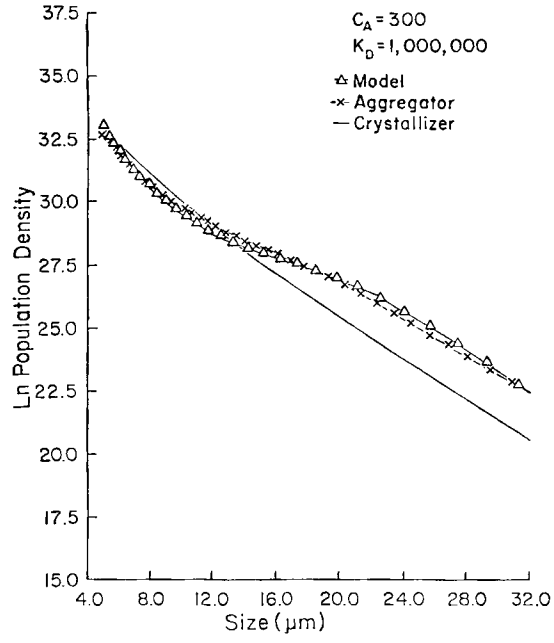

Figure 3. Comparison of calculated model distribution with experimental aggregator distribution at 250 rpm, 0.6 mM.

Experiment 3/24B, population density expressed in volume coordinates.

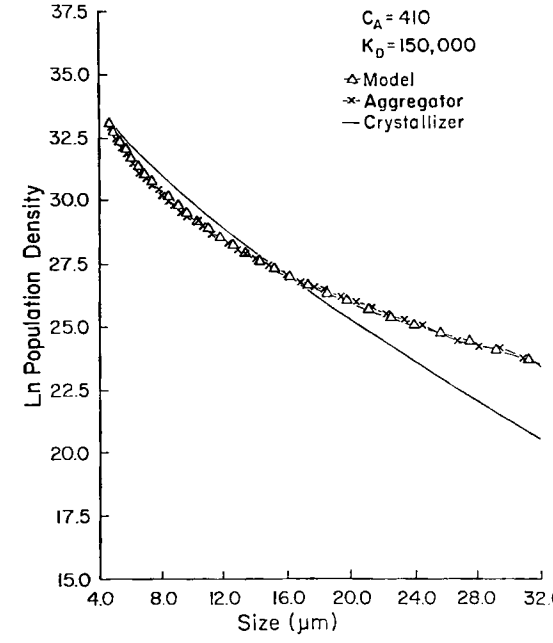

Figure 5. Comparison of calculated model distribution with experimental aggregator distribution at 150 rpm, 1.2 mM.

Experiment 5/14, population density expressed in volume coordinates.

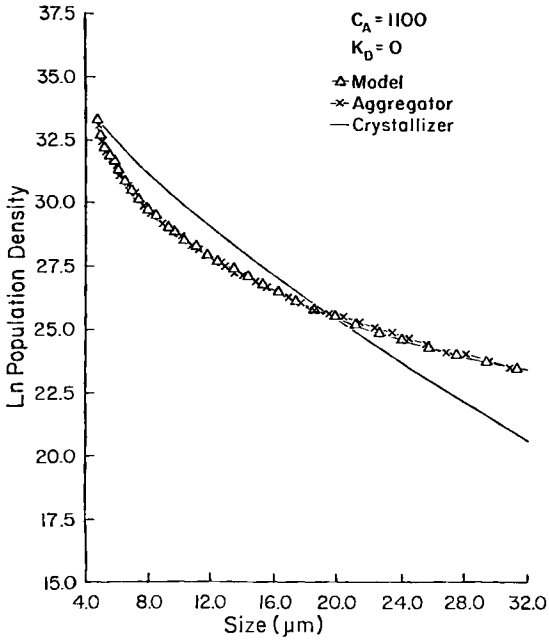

Figure 6. Comparison of calculated model distribution with experimental aggregator distribution at 150 rpm, 1.8 mM.

Experiment 5/25, population density expressed in volume coordinates.

Table 2. Kinetic Modeling Results of Inner Cylinder RPM Series

Experiment	RPM	[Ox]* mM	C_A 1/s	K_D 1/mL · s	B_u 1/mL² · s	ϕ**
3/14A	80	0.6	230	$5(10^5)$	$3(10^{11})$	16.01
3/14B	80	0.6	250	$1.5(10^5)$	$35(10^{11})$	3.00
3/17	80	0.6	290	$1.5(10^5)$	$5(10^{11})$	3.35
3/21	80	0.6	320	$3.7(10^5)$	$5(10^{11})$	4.02
4/1	120	0.6	200	$4(10^5)$	$1(10^{10})$	5.15
4/2A	120	0.6	260	$4(10^5)$	$1(10^{11})$	4.59
4/2B	120	0.6	320	$4.2(10^5)$	$3.5(10^{11})$	1.31
3/22	150	0.6	300	$5(10^5)$	$5(10^{10})$	0.89
3/23A	150	0.6	280	$5(10^5)$	$2(10^{11})$	2.06
3/23B	150	0.6	290	$6.7(10^5)$	$2.5(10^{11})$	0.86
4/14A	175	0.6	280	$8(10^5)$	$1(10^{10})$	1.63
4/14B	175	0.6	280	$9(10^5)$	$1(10^{10})$	1.62
4/15	175	0.6	240	$7.5(10^5)$	$2(10^{10})$	1.67
4/12B	200	0.6	280	$8(10^5)$	$1(10^{10})$	3.79
4/13A	200	0.6	275	$9(10^5)$	$1.5(10^{10})$	1.65
4/13B	200	0.6	310	$1(10^6)$	$5(10^{11})$	4.09
10/6	200	0.6	300	$1.5(10^6)$	$1(10^9)$	3.76
10/25	200	0.6	280	$1.5(10^6)$	0	4.76
10/27	200	0.6	165	$1(10^6)$	$1(10^{10})$	2.59
3/24B	250	0.6	300	$1(10^6)$	$5(10^{11})$	2.05
3/25	250	0.6	270	$7(10^5)$	$2(10^{11})$	3.47
3/26A	250	0.6	270	$7(10^5)$	$3(10^{11})$	2.64
3/26B	250	0.6	230	$6(10^5)$	$1.5(10^{11})$	3.82
10/13	250	0.6	200	$1(10^6)$	$1(10^{10})$	10.90

*Expressed as equivalent initial concentration.
**$\phi = \sum_{i=5}^{30sm} \{[\ln (n_A)_i - \ln (n_p)_i]^2\}$

Table 3. Kinetic Modeling Results of Oxalate Concentration Series

Experiment	RPM	[Ox]* mM	C_A 1/s	K_D 1/mL · s	B_u 1/mL² · s	ϕ**
3/22	150	0.6	300	$5(10^5)$	$5(10^{10})$	0.89
3/23A	150	0.6	280	$5(10^5)$	$2(10^{11})$	2.06
3/23B	150	0.6	290	$6.7(10^5)$	$2.5(10^{11})$	0.86
5/3	150	0.8	295	$3.7(10^5)$	$8(10^{10})$	2.26
5/8	150	0.8	300	$3.3(10^5)$	$1(10^{11})$	1.14
5/9A	150	0.8	360	$3.5(10^5)$	$3.5(10^{11})$	3.53
5/9B	150	1.0	380	$3.5(10^5)$	$4.5(10^{11})$	0.88
5/10	150	1.2	430	$1.6(10^5)$	$1(10^{12})$	0.97
5/11	150	1.2	410	$1.5(10^5)$	$2(10^{11})$	0.89
5/12A	150	1.4	810	$2(10^5)$	$1.5(10^{12})$	6.44
5/12B	150	1.4	850	$1(10^5)$	$3(10^{12})$	5.81
5/16B	150	1.6	930	0	$5(10^{12})$	2.60
5/17A	150	1.8	1400	0	$2(10^{13})$	0.98
5/17B	150	1.8	1500	0	$5(10^{13})$	2.63
5/25	150	1.8	1100	0	$1(10^{13})$	0.53
6/18	200	1.0	180	$2.5(10^5)$	$5(10^{10})$	1.92
6/19	200	1.8	500	0	$1.5(10^{12})$	1.26

*Expressed as equivalent initial concentration.
**$\phi = \sum_{i=5}^{30sm} \{[\ln (n_A)_i - \ln (n_p)_i]^2\}$

caused mainly by the change in the disruption rate of newly formed aggregates as shown in Figure 8. Here it is seen that the disruption rate increased dramatically as the agitation level increased.

In contrast, the aggregation parameter, C_A, increased dramatically as the oxalate concentration in the aggregator was increased. Figure 9 shows this increase. At the same time, the disruption parameter, K_D, decreased down to zero at the highest

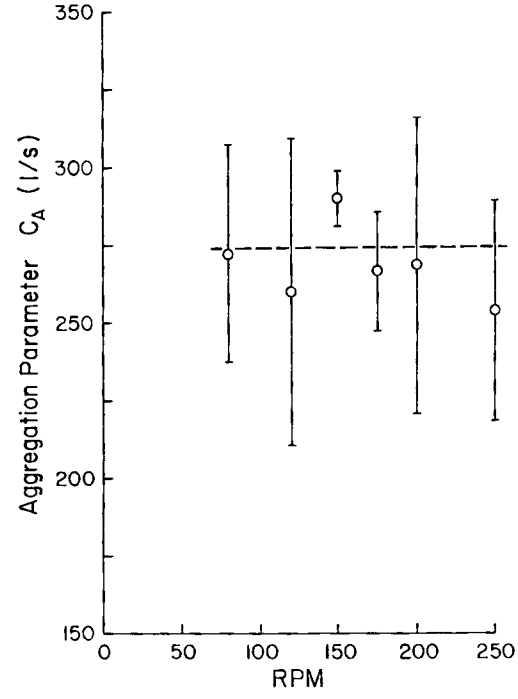

Figure 7. Variation of aggregation parameter, C_A, with inner cylinder rpm.

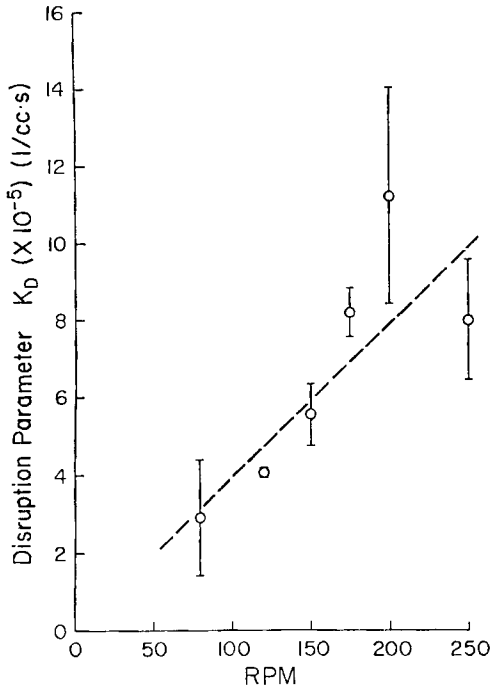

Figure 8. Variation of disruption parameter, K_D, with inner cylinder rpm.

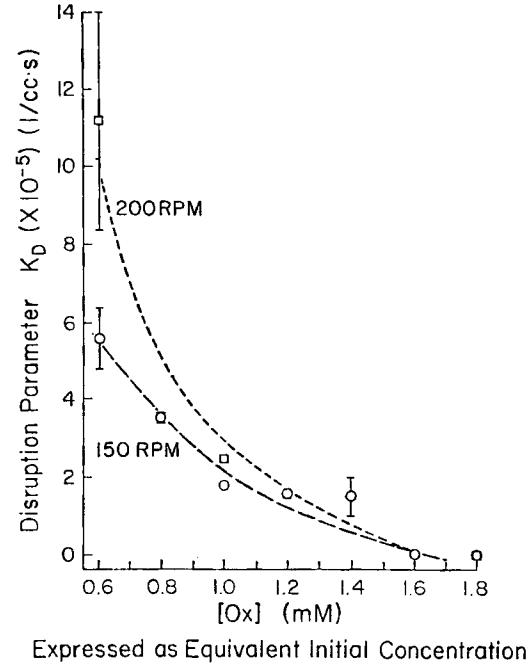

Figure 10. Variation of disruption parameter, K_D, with oxalate concentration in aggregator.

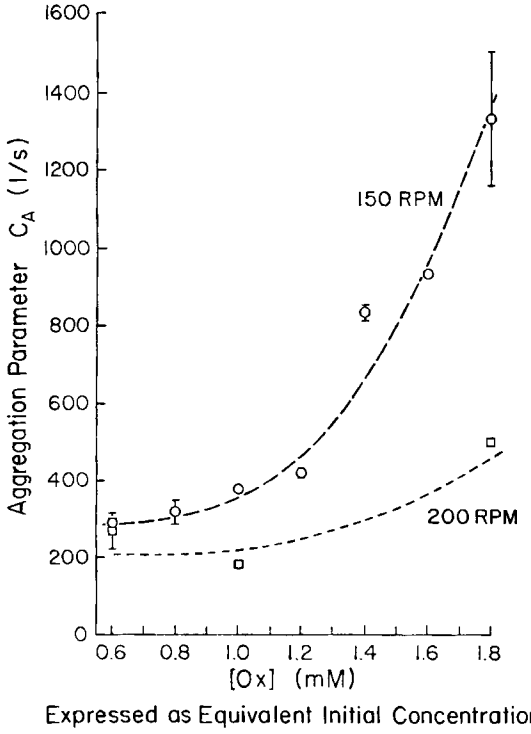

Figure 9. Variation of aggregation parameter, C_A, with oxalate concentration in aggregator.

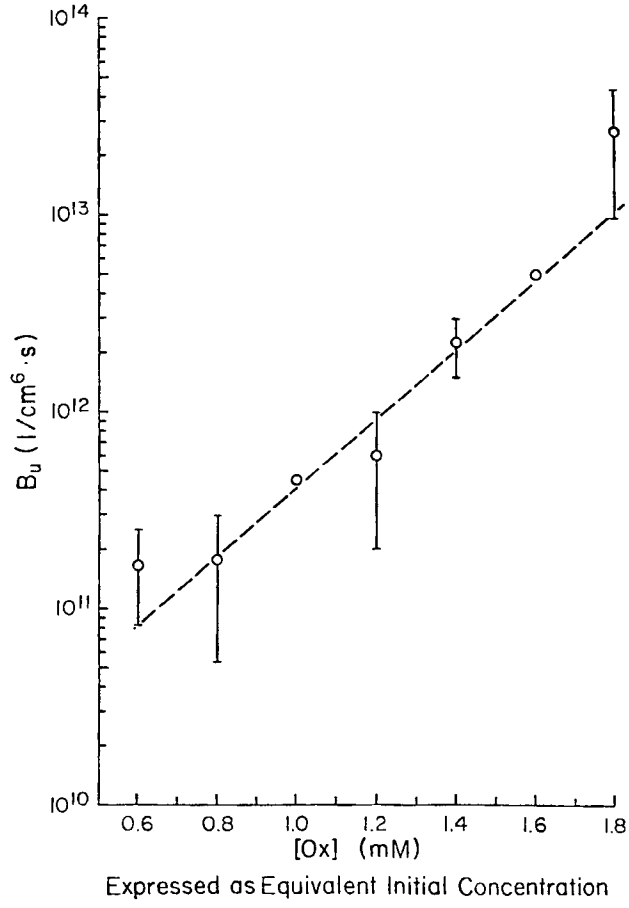

Figure 11. Variation of source function, Bu, with oxalate concentration in aggregator.

levels of oxalate, as seen in Figure 10. Figure 11 shows that the source function, B_u, increased exponentially as the oxalate concentration increased.

From the experiments performed at 200 rpm and higher oxalate levels, several observations can be made. Aggregation was more affected by the rpm level at the highest Ox concentrations than at the lowest levels. At the same time, the disruption rate was more affected by rpm at the lower oxalate concentrations.

Discussion

In general, the match between modeled and experimental distributions was quite good. This indicates that the aggregation and disruption phenomenon can be modeled adequately using the form of the population balance equation given in Eq. 14 for the range of rpm and oxalate concentration studied.

The form of the aggregation kernel given in Eq. 10 was found to match the experimental distributions over the range of conditions studied. While it is an empirical formulation, it does have a similar volume functionality as the turbulent inertial mechanism and the gravitational coagulation formulation of Berry (1967) without having the discontinuity of the first derivative. Therefore it becomes a more manageable formulation for numerical analysis. The volume (or size) dependency of the aggregation kernel can be shown by plotting K/C_A as a function of one particle's volume, v (or d_v), at various values of the second particle volume, u (or d_u). Figure 12 shows the size dependency of K/C_A for the empirical kernel of Eq. 10, which was used in the numerical calculations of this study. It is seen that the size dependency of the aggregation kernel goes to zero as d_u approaches d_v, indicating that the aggregation rate for equal-size particles is zero for this model. The size dependency of the turbulent inertial mechanism given by

$$K(u, v) = C_A (d_v + d_v)^2 \left| d_u^2 - d_v^2 \right| \qquad (15)$$

is quite similar, the main difference being the rate at which K/C_A approaches zero when $d_u = d_v$. This results in the discontinuity of the derivative at $d_u = d_v$. In contrast, the size dependency of the laminar shear field aggregation kernel shows a markedly different dependency with K/C_A increasing monotonically with particle size. From this analysis, it appears that aggregation in the Couette-flow apparatus under these conditions could be described by an empirical aggregation kernel that has a volume functionality similar to that proposed for turbulent coagulation by an inertial mechanism. According to Levich (1962), however, this mechanism is unlikely to be the cause of coagulation of colloids in liquids unless the density difference between particle and fluid is extremely large. This is not the case for calcium oxalate crystals in urinelike solutions. Further research is necessary to determine the actual mechanism of aggregation under these conditions.

The simple disruption functions given in Eqs. 12 and 13 have been shown to predict the experimentally determined decrease in population density at the larger sizes, particularly at the lower rpm. At 200 and 250 rpm, the form of the distribution becomes harder to model. This can be seen in Figure 3 for the distribution at 250 rpm. In general, at this rpm the model underpredicts the distribution between 8 and 16 μm and overpredicts between 20 and 28 μm. This is consistent with a breakage model that predicts a larger number of smaller particles than the simple two-body equal-volume breakage function. A more general form of the breakage function that includes integration over a fragment distribution would yield more accurate results at a cost of greater complexity. This problem is a topic of current research.

Figure 7 shows that the aggregation rate at the low oxalate concentration remained constant, within experimental error limits, as the rpm was increased from 80 to 250 rpm. However, the aggregation data with varying oxalate concentrations indicate that there was an rpm effect especially at the higher oxalate concentrations. This is seen in Figure 9, where the aggregation rates were different for the data at 150 and 200 rpm. There was a decrease in the aggregation rate at the higher rpm and this difference was amplified at higher oxalate concentrations. This is most likely attributable to increased disruption at the higher rpm. However, as the oxalate concentration increased, the aggregation rate increased dramatically. At the higher oxalate concentrations (increased supersaturation), the crystal growth rate is greater and bonding between crystals will occur more rapidly. In addition, the added oxalate ions will alter the electrostatic forces at the surface and/or compress the electrical double layer surrounding the crystal. The influence of each of these various effects must be studied further. This increased aggregation rate can also explain the data in Figure 11 where the source function, B_u, was found to increase with increasing oxalate concentration. The enhanced aggregation at the higher oxalate levels also caused the particles smaller than the 5 μm detection limit to aggregate more readily. Hence, they appear as an increase in mass in the aggregator distribution, and the source function increased as the aggregation rate increased.

It was shown in Part I that the flow in the aggregator annulus changed from a transitional laminar vortex flow to a turbulent vortex flow as the inner cylinder rotation rate was increased

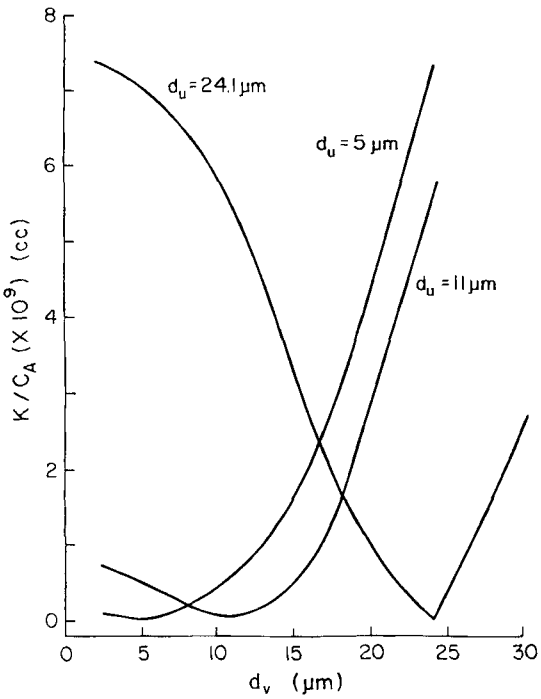

Figure 12. Size functionality of empirical aggregation kernel given by Eq. 10.

$K(u, v) = C_A (u - v)^2/(u + v) = C_A (d_u^3 - d_v^3)^2/(d_u^3 + d_v^3)$

from 80 to 250 rpm. The change in flow pattern occurred at approximately 150 rpm for the laboratory aggregator. As the turbulent intensity in the aggregator annulus increased with increasing rpm, the degree of rupture also increased. This is seen in Figure 8, where the disruption parameter, K_D, increased steadily with increasing rpm. The scatter in the data at the higher rpm was probably caused by a change from a predominantly two-body rupture to a multibody fragmentation caused by the higher turbulent intensities.

The decrease in the disruption parameter, K_D, seen in Figure 10 shows how the strength of the bond between particles became stronger as more oxalate ions were introduced. At both 150 and 200 rpm, the disruption rate had gone to zero when the oxalate concentration had reached about 1.6 mM. At 0.6 mM, the disruption effect of turbulent agitation was strong enough to rupture the bonds created between newly formed aggregates. However, at 1.6 mM, this was no longer true. The bond between particles had become strong enough to withstand the turbulent disruption intensity. At the higher oxalate concentrations, then, the coagulation mechanism becomes more agglomerationlike than aggregationlike.

These results have important implications in the formation of kidney stones. They suggest that in the range of parameters studied, the Ox concentration in the kidney has a much greater influence on the formation of aggregates than the hydrodynamic conditions. The turbulent intensity in the aggregator was certainly more energetic than the flow conditions in the kidney, suggesting that the oxalate concentration would play an even greater role in governing kidney stone formation. These kinetic observations are consistent with the importance given to control of oxalate concentration in the clinical treatment of CaOx stones.

Finally, the two-stage nucleator/aggregator together with the kinetics approach used appears to be a useful technique to quantitatively separate nucleation, growth, and aggregation in other crystallization systems.

Conclusions

1. Aggregation of CaOx nuclei can be modeled by numerical solution of the population balance equation with semiempirical formulations for the aggregation and disruption functions. Numerical distributions matched the experimentally determined aggregator distributions for varying flow conditions and oxalate concentrations.

2. An empirical aggregation kernel that is functionally similar to the theoretical formulation for a turbulent aggregation mechanism due to inertial collisions was found to reasonably model the experimental distributions. This kernel facilitated the numerical solution of the population balance equation.

3. Rupture of newly formed aggregates was modeled using a simple two-body equal-volume disruption model. A more complicated model would be necessary only at the highest levels of agitation.

4. The aggregation rate was independent of rpm at an oxalate level of 0.6 mM, but decreased with rpm at higher oxalate levels. The aggregation rate was found to increase dramatically as the oxalate level increased.

5. Higher turbulent intensity (higher inner cylinder rpm) resulted in an increased disruption rate of the newly formed aggregates. Higher oxalate concentrations resulted in lower disruption rates up to about 1.6 mM, where the disruption rate became zero, suggesting that the particles were becoming more like agglomerates than aggregates.

Acknowledgment

The kinetic analyses presented in this paper were based on the thesis data of Beth Gottung (1983) together with some supplementary data taken by Tochau Nguyen. Kinetic analysis was only made possible by the careful work of these two researchers. The writers are indebted to Miss Gottung for permission to use these data.

The writers are also indebted to Fred Gelbard for permission to use the extremely versatile particle simulator, program AEROSL. This work was supported by National Science Foundation Grant No. CPE-8117753.

Notation

B_a = birth rate of particles due to aggregation, no./mL^2 · s
B_d = birth rate of particles due to disruption, no./mL^2 · s
B_u = source function, no./mL^2 · s
C_A = aggregation parameter, 1/s
d_u = particle size corresponding to volume u, μm
d_v = particle size corresponding to volume v, μm
D_a = death rate of particles due to aggregation, no./mL^2 · s
D_d = death rate of particles due to disruption, no./mL^2 · s
E_i = collection efficiency in aggregation kernel
G_v = volume growth rate, mL/s
k_1 = constant in aggregation kernel
$K(u, v)$ = aggregation kernel, mL/s
K_D = disruption parameter, 1/mL · s
$n(v, t)$ = population density distribution function, no./mL^2
n_i = initial population density distribution function, no./mL^2
n_A = population density distribution of aggregator, no./mL^2
n_p = population density distribution predicted by model, no./mL^2
Sh = shear rate, 1/s
t = time, s
T = temperature, K
u = particle volume mL
$\dot{U}$ = velocity gradient, 1/s
v = particle volume, mL
v_a = Lowest measurable particle volume, mL

Greek letters

$\delta(v - v_a)$ = Dirac delta function
ϵ = rate of energy dissipation per unit mass, erg/g · s
κ = Boltzmann's constant
μ = fluid viscosity, mPa · s
ν = kinematic viscosity, cm^2/s
ρ = particle density, g/mL
ρ_o = fluid density, g/mL
τ = average residence time in aggregator, s
ϕ = logarithmic sum-of-squares difference function

Literature cited

Berry, E. X., "Cloud Droplet Growth by Collection," *J. Atmos. Sci.*, **24**, 688 (1967).

Drake, R. L., "A General Mathematical Survey of the Coagulation Equation," *Topics in Current Aerosol Research, Pt. 2*, G. M. Hidy and J. R. Brock, eds., Pergamon, New York (1972).

Gelbard, F., *AEROSL Users Manual*, Sandia Nat. Lab., NUREG/CR-1367, SAND80-0403, R7 (Mar., 1981).

Gelbard, F., and J. W. Seinfeld, "Numerical Solution of the Dynamic Equation for Particulate Systems," *J. Comp. Phys.*, **28**, 357 (1978).

Gottung, B. E., "Calcium Oxalate Agglomeration in Urinelike Mother Liquors," M.S. Thesis, Univ. Arizona, Tucson (1983).

Levich, V. G., *Physiochemical Hydrodynamics*, Prentice-Hall, Englewood Cliffs, N.J., pp. 213–219 (1962).

Low, G. C., "Agglomeration Effects in Aluminum Trihydroxide Precipitation," Ph.D. Diss., Univ. Queensland, Australia (1975).

Petanate, A. M., and C. E. Glatz, "Isoelectric Precipitation of Soy Protein. II: Kinetics of Protein Aggregate Growth and Breakage," *Biotech. Bioeng.*, **25,** 3,049, and **25,** 3,059 (1983).

Randolph, A. D., "Effect of Crystal Breakage on Crystal Size Distribution in a Mixed-Suspension Crystallizer," *IEC Fund.*, **8,** 58 (1969).

Randolph, A. D., and M. A. Larson, *Theory of Particulate Processes,* Academic Pr., New York, pp. 121–126, (1971).

Shampine, L. F., and M. K. Gordon, *Computer Solution of Ordinary Differential Equations, The Initial Value Problem,* Freeman (1975).

Smoluchowski, M .V., "Mathematical Theory of the Kinetics of the Coagulation of Colloidal Solutions," *Z. Phys. Chem.*, **92,** 129 (1917).

Swift, D. L., and S. K. Friedlander, "The Coagulation of Hydrosols by Brownian Motion and Laminar Shear Flow," *J. Colloid Sci.*, **19,** 621 (1964).

Thompson, P. D., "A Transformation of the Stochastic Equation for Droplet Coalescence," *Proc. Int. Conf. Cloud Physics,* Toronto, pp. 115–126 (1968).

Manuscript received Oct. 16, 1984, and revision received Oct. 21, 1985.